Journal of Materials Chemistry A

Accepted Manuscript

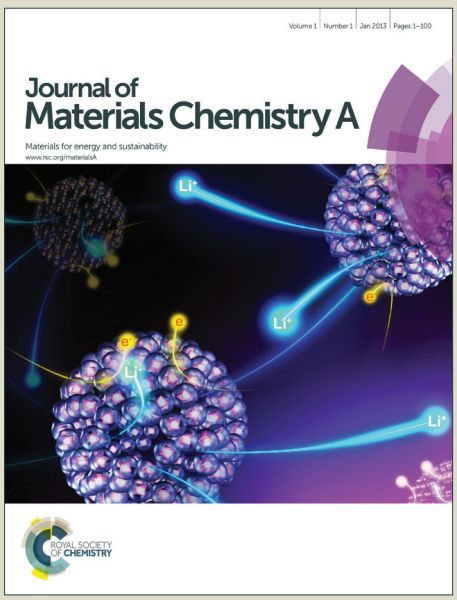

ROYAL SOCIETY OF CHEMISTRY

www.rsc.org/materialsA

Facile preparation of hierarchical Nb_2O_5 microspheres with photocatalytic activities and electrochemical properties

Sheng-qi Guo,[†] Xiao Zhang,[†] Zhen Zhou,*[,‡] Guan-dao Gao,*[,†] Lu Liu*[,†]

[†] *Tianjin Key Laboratory of Environmental Remediation and Pollution Control, Nankai University, Tianjin 300071, China.*

[‡] *Institute of New Energy Material Chemistry, Key Laboratory of Advanced Energy Materials Chemistry (Ministry of Education), Nankai University, Tianjin, 300071, China.*

KEYWORDS: hierarchical structure, Nb_2O_5, Ostwald ripening process, photocatalytic avtivity, lithium ion battery

Author information

* Corresponding author.

E-mail: zhouzhen@nankai.edu.cn; gaoguandao@nankai.edu.cn; liul@nankai.edu.cn.

Abstract: Hierarchical flower-like Nb_2O_5 microspheres have been prepared *via* a facile hydrothermal approach without any additives. X-ray diffraction (XRD), X-ray photoelectron spectroscopy (XPS), scanning electron microscopy (SEM), and transmission electron microscopy (TEM) were employed to clarify the structure and morphology of the Nb_2O_5 microspheres. The structure and morphology evolution mechanism have been proposed for the hierarchical structure in detail. During the symmetric Ostwald ripening, the resultants formed aggregates constructions composed of two-dimensional nanoflakes building blocks. Photocatalytic activity of the as-prepared Nb_2O_5 microspheres was evaluated by the photodegradation of Rhodamine B (RhB), and over 90% of RhB was degraded within 30 min under the irradiation of UV light. The as-prepared Nb_2O_5 exhibits higher photocatalytic activity than commercial Degussa P25. Moreover, Nb_2O_5 was tested as anode materials of lithium ion batteries, which displayed high reversibility and excellent rate stability at current density 50 mAg^{-1}.

1. Introduction

The rational design and synthesis of inorganic nanomaterials with hierarchical structure have attracted a great deal of attention in the past few decades.[1-5] To date, several excellent reviews about hierarchical structure in natural science have been published following a summary compilation by Waller in 1976.[6-8] The analysis of data for existing materials reveals that hierarchical structure materials, especially curved three-dimensional (3D) microspheres, which possess dual or multiple morphologies and structures are greatly important for performance improved and further realizing widely potential application.[9-12] In 2011, Fu group[13] and Sun group[14] reported different kinds of hierarchical flower-like TiO_2 microspheres in succession, and they demonstrated that the materials had better photocatalytic activity and higher photoelectric conversion efficiency than P25, respectively. In addition, our group also dedicated to the research in design and synthesis of hierarchical structure materials, and we had prepared a series of hierarchical microspheres materials in the past years, which exhibit interesting electrical properties.[15,16] So far, some examples of transition metal oxides with 3D hierarchical microspheres architectures have been obtained, such as Fe_3O_4,[17,18] MoO_2,[19] CuO[20] and Co_3O_4.[21] However, compared to those well-reported transition metal oxides, there is an unfavorable lack of investigation on niobium oxides with hierarchical nanostructures.

As the most thermodynamically stable phase in niobium oxides,[22] diniobium pentaoxide (Nb_2O_5) has been considered for applications in diverse fields involving gas sensing,[23] catalysis,[24] and as electrochromic material.[25] As we know that the valuable functions greatly depend on the size and structure. Thus, nanostructure Nb_2O_5 with controlled morphologies has become favorable due to their unique properties such as larger surface area and accelerated phase transitions. Up to now, a few studies focused on the nanostructures of Nb_2O_5 including nanoplates,[26] nanowires,[22,27] nanorods[28], nanotubes[29] and nanopore[30,31] had been reported. However, to our knowledge, there is no report on the fabrication of Nb_2O_5 with hierarchical nanostructures.

In this study, we have successfully developed a concise way to synthesize flower-like hierarchical Nb_2O_5 microspheres under hydrothermal conditions without any additives. The possible formation mechanism is rationally proposed for the time and alkaline-dependent experiments. To explore the functionality of this material, we have investigated the photocatalytic activities of Nb_2O_5, which exhibits significantly enhanced photocatalytic activity in the degradation of aqueous RhB. Furthermore, with stable cycling performance as anode electrode materials, Nb_2O_5 microspheres display potential application in LIBs.

2. Experimental details

Preparation of hierarchical Nb_2O_5 microspheres. All reagents are of analytic grade and were used without further purification. In a typical synthesis, a mixture of $NbCl_5$ (0.2g) and Hexamethylenetetramine (0.4g) in water was stirred for 30 min, and then sealed in a 30ml Teflon-lined stainless steel autoclave and heated at 180°C for 24 h. After the sample was gradually cooled to room temperature, a white precipitate was collected and then washed with distilled water and absolute ethanol, and the sample was kept in absolute ethanol.

Material Characterization. X-ray diffraction analysis of the samples were carried out by an X-ray diffractometer (XRD, Rigaka D/max2500) with Cu Kα radiation (λ = 1.54056 Å). The morphology of the as-prepared products was characterized by scanning electron microscopy (SEM, Hitachi-530 or JEOLJSM-6700F) and transmission electron microscopy (TEM, JEOL-2010, operating voltage of 200 kV). The elemental composition was detected by X-ray photoelectron spectroscopy (XPS, Kratos Axis Ultra DLD). The Brunauer−Emmett−Teller (BET) specific surface area (SBET) of the sample was analyzed by nitrogen adsorption in a Tristar 3000 nitrogen adsorption apparatus, UV spectra were recorded on a Cary 5000 spectrometer at room

temperature.

Photocatalytic Reactions. The photocatalytic activities of the as-prepared Nb_2O_5 hierarchical structures were evaluated by the photocatalytic degradation of RhB aqueous solution via an XPA-system Photochemical Reactor (Nanjing, China) at room temperature under ultraviolet light irradiation. A 300 W Hg arc lamp was used as a light source to provide the UV light. In a typical reaction, 0.1 g of as-prepared photocatalysts was dispersed into 100 mL of RhB aqueous solution (1×10^{-5} M). Before light irradiating, the suspension was stirred for 30 min in the dark to reach adsorption equilibrium of RhB on the surface of photocatalysts. Then, the reaction was stopped at 30 min intervals and 10 mL of reaction solutions were extracted to determine the concentrations of the aqueous RhB solution by UV/vis spectroscopy. In this study, P25 was used as control to photocatalytic RhB under the same condition as the as-prepared samples. RhB aqueous solution without photocatalysts irradiated by UV light was used as a blank experiment and the as-prepared photocatalysts reacting with RhB in dark were used as comparative evaluation.

Electrochemical Measurements. In test cells, lithium metal was used as the counter and reference electrode. The working electrodes were composed of active materials, acetylene black (AB), and polytetrafluoroethylene (PTFE) at the weight ratio of 15:4:1. The weight of the working electrode was 2.3 mg. The electrolyte was 1 M LiPF6 dissolved in a 1:1:1 mixture of ethylene carbonate (EC), ethylene methyl carbonate (EMC), and dimethyl carbonate (DMC). The cells were assembled in a glove-box filled with high-purity argon. Discharge / charge measurements of the cells were performed at different current densities between the potentials of 0.01-3.00 V (vs Li^+ / Li) under a LAND-CT2001A battery tester.

3. Results and discussion

Structure and Morphology. X-ray diffraction was used to characterize the phase structure of the products. Figure 1 shows the powder XRD patterns of the as-prepared samples. All the peaks in Fig. 1 can be readily indexed as pure orthorhombic Nb_2O_5, which is in good agreement with the values from the standard card (JCPDS, file No. 20-804).[28] Compared with those of the bulky counterpart, the peaks are relatively broadened, which reveals that the nanoflakes have very small crystal sizes. From Figure 1, it can be observed that (1 1 3) plane is unusually stronger than the corresponding conventional values. This observation indicates that the resultant Nb_2O_5 products

are mainly dominated mainly dominated by (1 1 3) plane, therefore, the (1 1 3) plane tend to be preferentially oriented parallel to the surface of the supporting substrate in the experiment.[32,33] Further evidence for the composition was obtained by XPS. Figure 2 shows the typical XPS spectra taken from the niobium and oxygen regions of the products. The two peaks located at 207.9 and 210.6 eV are attributed to Nb_{3d} and that at 531.0 eV corresponds to O_{1s}. The ratio of Nb to O is approximately 1:2.58, which reveals that the sample has high purity.

/*Insert Figure 1.*/

/*Insert Figure 2.*/

/*Insert Figure 3.*/

The morphologies of the resulting Nb_2O_5 sample were first investigated by scanning electron microscopy (SEM). Figure 3a and 3b show the representative that the products are composed of a large quantity of flower-like structures, with an average diameter of 1.2 μm. Higher magnification microscopy exhibits detailed front surface information of the particular architecture, which is constructed by distorted nanoflakes with thickness of 30 nm in three directions. In addition, the sample was characterized by TEM, (Fig. 3c and 3d) and the low-magnification TEM images further clearly indicate that the sample is composed of aggregated nanoflakes. Especially, it is more obvious that the edge portion of the superstructure is lighter than that of the center. The high-resolution TEM images (Fig. 3d) show that the crystalline lattice distances in the white frame are 3.59 Å, corresponding to the (0 0 4) planes of Nb_2O_5 which are consistent with the XRD results. Moreover, the N_2 physisorption measurements isotherms for the sample is characteristic of a typical type IV isotherm with H1 hysteresis loop based on Brunauer-Deming-Deming-Teller (BDDT) classification (Fig. 4), which is indicated by a hysteresis loop at high relatively pressures associated with capillary condensation of gases within mesopores in the size range of 2-50 nm.[29] The BET surface area is 86.81 m^2g^{-1} and the pore-size distribution curve obtained through the BJH method suggests that most pores showed the sizes of 3.5 nm.

/*Insert Figure 4.*/

Formation Mechanism. In order to investigate the evolution of the flower-like Nb_2O_5 microspheres, we first carried out the time-dependent synthesis and investigated the products at different stages by XRD and SEM techniques. From the XRD patterns in Fig. 5e, it is clearly observed that the formation of Nb_2O_5 is very fast, after reacting for just 2h. And the products

collected at every time interval are almost consistent with the product obtained at 24 h. Fig. 5b–d shows the morphological evolution from irregular shapes at the beginning to the final flower-like aggregates. There is no product collected at the initial 8 h reaction. Prolonging reaction time to 16 h, the intermediates close to the final morphology assembled by nanoflakes appear but there exists some nanoparticles as observed. As the reaction proceeds to 24 h, the typical flower-like microstructure has been formed. Comprehensive series of experimental phenomna, we could conclude that time is one of the most important controlling factor in the formation process.

/*Insert Figure 5.*/

We also investigated the effect of alkaline on the morphology of Nb_2O_5 microspheres. We conducted the alkaline-dependent experiments by changing the amount of hexamethylenetetramine while the reaction time and temperature was fixed at 24 h and 180 ºC, respectively. With the assistance of low concentration of hexamethylenetetramine (0.2g), the products have no regular shapes (Fig. S1a). The increase of the amount of hexamethylenetetramine could improve the yield and quality of 3D aggregates. As shown in Figure 3, when 0.4 g of hexamethylenetetramine was used, the sample is consisted of aggregates with regular morphologies and in uniform size. With the continue increase of alkali source, flower-like aggregates could also be obtained, but products contains defective flower-like balls and irregular 3D aggregates (Fig. S1). Furthermore, we tried to use other alkali source in this system, there is no regular product collected if hexamethylenetetramine is replaced by NaOH or Na_2CO_3 (Fig. S2). Note that, when Na_2CO_3 was used as the alkali source, the phase of Nb_2O_5 changed from orthorhombic space group C2/m to monoclinic space group Pbam. This change could be confirmed through XRD. A series of results reveal that the source and amount of an appropriate alkaline is indispensable in forming and keeping the characters and shapes of precursor microspheres during the calcination process.

On the other hand, we investigated influences of temperature on the final structures of Nb_2O_5. The elaborate temperature experiments were carried out, which shows that lower reaction temperature is not conducive to the formation of hierarchical Nb_2O_5 microspheres. The related XRD patterns and SEM images are shown in Fig. S3.

On the basis of the above results, we can propose a growth process of the 3D hierarchical microspheres with Nb_2O_5 2D nanoflakes assembly. Firstly, the hydrolysis of the

hexamethylenetetramine results in the formation of OH^- ions, which provide a weak basic environment for the formation of Nb_2O_5 crystal nucleus. Then, adjacent Nb_2O_5 crystal nucleuses may attach to each other and gather into colloidal irregular aggregates to reduce surface area and surface energy. With the occurrence of anisotropic process, the irregular aggregates may further coagulate to form ordered hierarchical 3D microspheres, which were constructed by nanoflakes. The whole formation process of hierarchical Nb_2O_5 microspheres is illustrated in Figure 5a. Generally, two key stages are involved during this morphological transformation: nucleation and Ostwald ripening. In this reaction system, the Nb_2O_5 nanoparticles firstly grew into aggregates with irregular shapes through nucleation following its crystal growth habit, and then evolved into flower-like Nb_2O_5 aggregates *via* Ostwald ripening.

Photocatalytic performances. The UV-vis absorption spectra of Nb_2O_5 microspheres in ambient temperature is shown in Fig. 6a, a strong absorption can be observed in the ultraviolet region for the as-prepared Nb_2O_5. The band gap energies of Nb_2O_5, 3.4 eV, can be reckoned from the plot of transformed Kubelka–Munk function versus the energy of exciting light.[34] Photocatalytic activities of the as-prepared Nb_2O_5 under UV light were examined by typical photodegradation experiments of aqueous RhB, where Degussa P25 TiO_2 was used as a reference photocatalyst, the results are shown in Figure 6b and 6c. The characteristic wavelength of RhB absorption is 553 nm, and the area of the absorption peak correlates well with the RhB concentration. With the increase of illumination time, the main absorption peak gradually weakened and completely disappears after about 60 min. No other absorption bands appear in either the ultraviolet or visible region. Time course of the decrease in the dye concentration using different catalysts is shown in Figure 6c, where all of the reaction time was deducted the time of adsorption equilibrium. After 30 min, 90% RhB was almost degraded by as-prepared photocatalyst, which is much more than that of P25 (nearly 45%). After 60 min of UV light irradiation, nearly all RhB was removed by the as-prepared Nb_2O_5 while only 83% RhB was removed by P25. In Nb_2O_5 system, although the band gap is larger than that of TiO_2 (3.2 eV), which means less UV light can be harvested. Obviously, the as-prepared Nb_2O_5 exhibits better photocatalytic activity than P25. This is mainly attributed to the large BET surface area of Nb_2O_5 (86.81 m^2g^{-1}), much more than that of P25 (50 m^2g^{-1}), which is favorable to increasing the photocatalytic reaction sites. In particular, mesoporous structure of the catalyst bring on light waves to penetrate deep inside the

photocatalyst and beget high mobility of charge, which also lead to higher catalytic activity.[35-37]

Also, the photocatalyst stability besides the photocatalytic activity is very important in the practical application. Thus, recycle experiments was further investigated. As shown in Fig. S4, the hierarchical microsphere photocatalysts did not exhibit any significant loss of activity after three recycles for the photodegradation of RhB, indicating that these photocatalysts is anti-photo corrosion during the photocatalytic oxidation of the dye molecules.

/*Insert Figure 6.*/

The radicals and holes trapping experiments were also designed to elucidate the photocatalytic degradation process of Nb_2O_5. Herein, Isopropyl alcohol and EDTA have been selected as ·OH radicals and hole scavengers, respectively. As shown in Figure 6d, the photodegradation rate of RhB is slightly suppressed in Nb_2O_5—EDTA system, whereas it is obviously inhibited in Nb_2O_5—Isopropyl alcohol system. This means that the ·OH radicals could be the main active oxygen species that can oxidize the adsorbed organic pollutants. According to the literature,[26,38] photocatalytic activity is governed by various factors such as crystallinity, band gap, and surface properties. For Nb_2O_5 catalyst, the great photocatalytic activity should be attributed to its special structural features.[39] The hierarchical microsphere structure would effectively prevent overlap between nanoflakes and thus maintain a large active surface area,[40] this implies Nb_2O_5 can harvest more UV light to produce enough ·OH radicals as one of strongest oxidant known, which could oxidize directly the organic pollutants (reactions 1-3). In addition, large surface area of hierarchical Nb_2O_5 microspheres leads to both more surface reaction sites for the adsorption of reactants molecules and more surface hydroxyl groups, these surface hydroxyl groups, which not only could accept photogenerated holes to prevent electron-hole recombination,[41] but also provide conditions for subsequent produce ·OH radicals (reaction 4).[42] In one word, the higher photodegradation rate in the Nb_2O_5 had been primarily ascribed to the porous hierarchical structure.

$$Nb_2O_5 + \text{ultraviolet light} \rightarrow h^+ + e \qquad (1)$$

$$h^+ + H_2O \rightarrow \cdot OH + H^+ \qquad (2)$$

$$\cdot OH + h^+ + \text{organic pollutants} \rightarrow \text{product} \qquad (3)$$

$$OH^- + h^+ \rightarrow \cdot OH \qquad (4)$$

Compared to P25, although the as-prepared Nb_2O_5 exhibits higher photocatalytic activity, it is

more expensive. Therefore, we tried to reduce the amount of Nb_2O_5, and dosage effect experiments were carried out. The results are shown in Figure S5. Fortunately, when reduced the amount of Nb_2O_5 to 1/2 of TiO_2 for photocatalysis, the as-prepared Nb_2O_5 exhibits better photocatalytic activity than P25. So we believe that the hierarchical flower-like Nb_2O_5 microsphere is efficient for the environmental purification of organic pollutants in aqueous solution.

Electrochemical Performances. To investigate the lithium storage performances of the obtained Nb_2O_5 microspheres, working electrode was assembled in cells and tested in the voltage range of 0.01-3.00 V at 50 mAg^{-1}. Figure 7a shows the charge–discharge curves of the electrode made from the hierarchical Nb_2O_5 microspheres. In the initial cycle, there is no obvious platform observed and the electrochemical reactions of Nb_2O_5 with lithium involve multi-steps for its decomposition and formation from the curve. It's noteworthy that the initial cycle shows high discharging capacity of 962 $mAhg^{-1}$, while the capacity decreases to 391 $mAhg^{-1}$ in the second discharge. Such result probably is due to two reasons, firstly, the faradic contributions of side reaction with electrolyte and/or reversible formation of polymer/gel-like film through a so-called "pseudo-capacitance-type behavior".[43,44] Secondly, the irreversible reactions including the formation of the SEI film and further lithium consumption via interfacial reactions due to the charge separation at the metal/Li_2O phase boundary.[45-48] Moreover, during the subsequent cycles, the charge–discharge curves almost overlap, demonstrating excellent cycling stability.

To better understand the electrochemical behaviors of Nb_2O_5, cyclic voltammetry (CV) measurements were performed between 0.01 to 3.0 V at room temperature, with a scan rate of 0.5 $mV{\cdot}s^{-1}$ (Fig. 7b). An apparent cathodic peak at 0.55 V is observed in the initial discharge of Nb_2O_5 and vanishes in subsequent cycles, which corresponds to the reduction of Nb_2O_5 and the formation of SEI films. Initial anodic scan reveals one main peak around 1.5 V, and this peak exists in subsequent cycles. Generally, the first two cycles are the formation cycles, during these cycles good electrical contact between active material, binder, and conducting carbon and current collector is established.[49,50] Herein, the main cathodic and anodic peaks correspond to insertion/extraction of Li to/from the Nb_2O_5 lattice, the Li storage mechanism in Nb_2O_5 can be interpreted as $Nb_2O_5 + xLi^+ + xe^- \rightarrow Li_xNb_2O_5$, during lithiation and delithiation, the cathodic and anodic process follows the transition between Nb^{5+}/Nb^{4+}, and the theoretical capacity of

Nb_2O_5 should be calculated as 201.6mAh/g, corresponding to x=2 in $Li_xNb_2O_5$.[51] Furthermore, the subsequent CV curves (2nd and 3rd) overlap well, and reveal good reversibility of Li storage performances.

/*Insert Figure 7.*/

Cyclic stability. Figure 7c displays the cycling performance of the as-prepared Nb_2O_5 at a current rate 50 mAg^{-1}. A gradual loss of capacity from the early cycles is clearly observed, it is attributed to the irreversible reactions between active materials and electrolyte and the large volume changes occurred in the structure after the lithium inclusion, which may destroyed the SEI film on the iron oxide anodes.[47,50,53] However, the capacities degradation not further continues in subsequent cycles, it show a very high cycle stability from 8 (217.5 $mAhg^{-1}$) to 200 cycles (219.5 $mAhg^{-1}$). From the initial ten cycles, the Coulombic efficiency rapidly increased nearly 95%, whereas the reversible capacity remained 198 $mAhg^{-1}$ after 100 cycles with a negligible loss of only 0.06 % per cycle. When the rate is increased stepwise from 50 mAg^{-1} up to100, 200, 400, 800 mAg^{-1}, some stable capacity of about 124, 82, 62 and 39 $mAhg^{-1}$ can be achieved, respectively (Fig. 7d). Remarkably, when the current rate is again reduced to 50 mAg^{-1}, a stable high capacity of 180 $mAhg^{-1}$ can be resumed. We believe that the high reversibility and good rate stability are due to the unique hierarchical structure with preferable stability. Recently, Ma et al. have examined Nb_2O_5 with particles size varying around tens of nanometers with agglomeration as an anode material at a current density of 50 mAg^{-1},[54] it shows observed capacity decreasing trend in 50 cycles. In contrast, hierarchical Nb_2O_5 anodic exhibits even more remarkable cycle stability and reversibility than that one.

EIS is an effective method for evaluation of the electron conductivity and Li^+ diffusion of materials.[55] The EIS data was modeled using the *Zview* software and presented as red line in Figure 8a with the corresponding fitted parameters in Table S1. Fig. 8a also shows the equivalent circuit modeled from impendence spectra of Nb_2O_5 microspheres electrode. Herein, Rs (3.641Ω) is the resistance of the electrode, electrolyte and membrane. CPE and Rct (197.2Ω) represent the constant phase capacitance and the resistance, respectively, which produced from the reaction between the electrolyte and the surface of the electrode. In the impendence spectra, CPE and Rct are corresponding to the semicircle in the high-frequency range, which is attributed to Li migration through surface films at the electrode/electrolyte interface. Moreover, *W*o in the

equivalent circuit is Warburg impedance, it represents the diffusion of Li^+ within the bulk anode/electrode and corresponding to the inclined in the low-frequency range.

/*Insert Figure 8.*/

Fig. 8b shows the Nyquist plots of the Nb_2O_5 microspheres at different stages. Nb_2O_5 electrodes show only one semicircle in the high-frequency range and an inclined line in the low-frequency range in the stages of before cycling (i), after 1 cycle (iii) and 3 cycles (iv). Previous studies showed that the semicircle in the high-frequency region could reflect the charge transfer process at the conductive agent interface which dominates the reduction reaction during upper voltage plateau, while the inclined in the low-frequency range is corresponds to the Li^+ diffusion process.[56,57] Notably, the interfacial resistance is observed to decrease with the continuous cycles, it may attributed to pulverization of the Nb_2O_5 surface and a subsequent increase in the surface area that reduces the interfacial resistance.[58] Moreover, in the stage of the Nb_2O_5 electrodes after first discharge (ii), the EIS profile demonstrates two semicircles, the high-frequency semicircle is assigned to the formation of SEI film,[59-61] which mainly grows in the initial discharge process. The second semicircle is probably attributed to charge transfer kinetics.

4. Conclusions

In summary, a hierarchical flower-like Nb_2O_5 microsphere was obtained *via* a facile and template-free method. During the synthetic procedure the hydrolysis of the hexamethylenetetramine provided OH^- source was used to control the formation of 3D microspheres. The photocatalytic performance of the Nb_2O_5 nanostructures was evaluated by examining the degradation of RhB under UV light irradiation. In addition, when evaluated as anode materials for lithium-ion batteries (LIBs), Nb_2O_5 with the special structure displayed excellent cycle stability and reversibility. Furthermore, this material is also expected to have potential applications as gas sensing and electrodes for other electronic devices. Related work is in progress.

Acknowledgements

This work was supported by the National Science Foundation of China (No. 21271108), the Ministry of Science and Technology (Grant 2014CB932001), Tianjin Municipal Science and Technology Commission (Grant 12HZGJHZ01100), and China–U.S. Center for Environmental Remediation and Sustainable Development.

References

1. Z. W. Pan, S. M. Mahurin, S. Dai and D. H. Lowndes, *Nano Lett.*, 2005, **5**, 723–727.

2. H. Q. Yan, R. R. He, J. Johnson, M. Law, R. J. Saykally and P. D. Yang, *J. Am. Chem. Soc.*, 2003, **125**, 4728–4729.

3. C. L. Nehl, H. W. Liao and J. H. Hafner, *Nano Lett.*, 2006, **6**, 683–688.

4. M. H. Cao, T. F. Liu, S. Gao, G. B. Sun, X. L. Wu, C. W. Hu and Z. L. Wang, *Angew. Chem. Int. Ed.*, 2005, **44**, 4197–4201.

5. A. Parfenov, I. Gryczynski, J. Malicka, C. D. Geddes and J. R. Lakowicz, *J. Phys. Chem. B*, 2003, **107**, 8829–8833.

6. R. J. Waller, *Decision Sciences*, 1976, **7**, 659–674.

7. G. A. A. Soler-lllia, C. Sanchez, B. Lebeau and J. Patarin, *Chem. Rev.*, 2002, **102**, 4093–4138.

8. M. Heim, L. Römer and T. Scheibel, *Chem. Soc. Rev.*, 2010, **39**, 156–164.

9. X. L. Hu, Y. Masuda, T. Ohji and K. Kato, *Cryst. Growth Des.*, 2009, **10**, 626–631.

10. Y. Hou, H. Kondoh and T. Ohta, *Chem. Mater.*, 2005, **17**, 3994–3996.

11. B. B. Kale, J. O. Baeg, S. M. Lee, H. Chang, S. J. Moon and C. W. Lee, *Adv. Funct. Mater.*, 2006, **16**, 1349–1354.

12. X. M. Sun, J. F. Liu and Y. D. Li, *Chem. –Eur. J.*, 2006, **12**, 2039–2047.

13. G. H. Tian, Y. J. Chen, W. Zhou, K. Pan, C. G. Tian, X. R. Huang and H. G. Fu, *CrystEngComm*, 2011, **13**, 2994–3000.

14. F. Shao, J. Sun, L. Gao, S. W. Yang and J. Q. Luo, *ACS Appl. Mater. Interface*, 2011, **3**, 2148–2153.

15. L. Liu, Y. Li, S. M. Yuan, M. Ge, M. M. Ren, C. S. Sun and Z. Zhou, *J. Phys. Chem. C.*, 2010, **114**, 251–255.

16. L. Liu, H. J. Liu, H. Z. Kou, Y. Q. Wang, Z. Zhou, M. M. Ren, M. Ge and X. W. He, *Cryst. Growth Des.*, 2009, **9**, 113–117.

17. L. R. Kong, X. F. Lu, X. J. Bian, W. J. Zhang and C. Wang, *ACS Appl. Mater. Interfaces*, 2011, **3**, 35–42.

18. Y. J. Zhu and J. S. Xu, *ACS Appl. Mater. Interface*, 2012, **4**, 4752–4757.

19. X. F. Zhang, X. X. Song, G. Shan, Y. M. Xu, X. L. Cheng, H. Zhao and L. H. Huo, *J. Mater. Chem. A*, 2013, **1**, 6858–6864.

20. H. G. Yu, J. G. Y, S. W. Liu and S. Man, *Chem. Mater.*, 2007, **19**, 4327–4334.

21. H. Pang, F. Gao, Q. Chen, R. M. Liu and Q. Y. Lu, *Dalton Trans.*, 2012, **41**, 5862–5868.

22. B. Varghese, S. C. Haur and C –T. Lim, *J. Phys. Chem. C.*, 2008, **112**, 10008–10012.

23. Y. D. Wang, L. F. Yang, Z. L. Zhou, Y. F. Li and X. H. Wu, *Mater. Lett*., 2001, **49**, 277–281.

24. K. Taanabe, *Catal. Today*, 2003, **78**, 65–77.

25. N. Özer, D. G. Chen and C. M. Lampert, *Thin Solid Films*, 1996, **277**, 162–168.

26. S. X. Ge, H. M. Jia, H. X. Zhao, Z. Zheng and L. Z. Zhang, *J. Mater. Chem.*, 2010, **20**, 3052–3058.

27. A. L. Viet, M. V. Reddy, R. Jose, B. V. R. Chowdari and S. Ramakrishna, *J. Phys. Chem. C.*, 2010, **114**, 664–671.

28. R. Fiz, F. Hernandez-Ramirez, T. Fischer, L. Lopez-Conesa, S. Estrade, F. Peiro and S. Mathur, *J. Phys. Chem. C.*, 2013, **117**, 10086–10094.

29. J. G. Yu, J. J. Fan and K. L. Lv, *Nanoscale*, 2010, **2**, 2144–2149.

30. J. Z. Ou, R. A. Rani, M-H, Ham, M. R. Field, Y. Zhang, H. D. Zheng, P. Reece, S. Zhuiykov, S. Sriram, M. Bhaskaran, R. B. Kaner and K. Kalantar-zadeh, *ACS Nano*, 2012, **6**, 4045–4053.

31. R. A. Rani, A. S. Zoolfakar, J. Subbiah, J. Z. Ou and K. Kalantar-zadeh, *Electrochem. Commun.*, 2014, 40, 20–23.

32. G. Li, M. Y. Liu and H. J. Liu, *CrystEngComm*, 2011, **13**, 5337–5341.

33. M. Y. Liu, G. Li and X. S. Chen, *ACS Appl. Mater. Interface*, 2014, **6**, 2604–2610.

34. S. Sakthivel and H. Kisch, *Angew. Chem. Int. Ed.*, 2003, **42**, 4908–4911.

35. X. C. Wang, J. C. Yu, C. M. Ho, Y. D. Hou and X. Z. Fu, *Langmuir*, 2005, **21**, 2552–2559.

36. C. S. Guo, M. Ge, L. Liu, G. D. Gao, Y. C. Feng and Y. Q. Wang, *Environ. Sci. Technol.*, 2010, **44**, 419–425.

37. L. Z. Zhang, and J. C. Yu, *Chem. Commun*., 2003, **16**, 2078–2079.

38. C. S. Pan and Y. F. Zhu, *Environ. Sci. Technol.*, 2010, **44**, 5570–5574.

39. D. Li, X. C. Duan, Q. Qin, H. M. Fan, W. J. Zheng, *J. Mater. Chem. A*, 2013, **1**, 12417–12421.

40. F. Lu, W. P. Cai and Y. G. Zhang, *Adv. Funct. Mater.*, 2008, **18**, 1047–1056.

41. S. Sato, *Langmuir*, 1988, **4**, 1156–1159.

42. M. M. Cheng, W. H. Ma, J. Li, Y. P. Huang, J. C. Zhao, Y. X. Wen and Y. M. Xu, *Environ. Sci. Technol.*, 2004, **38**, 1569–1575.

43. Y. R. Zhong, L. W. Su, M. Yang, J. P. Wei and Z. Zhou, *ACS Appl. Mater. Interface*, 2013, **5**, 11212–11217.

44. S. Laruelle, S. Grugeon, P. Poizot, M. Dollé, L. Dupont and J. M. Tarascon, *J. Electrochem. Soc.*, 2002, **149**, A627–A634.

45. J. Q. Yang, L. F. Jiao, Q. Q. Zhao, Q. H. Wang, H. Y. Gao, Q. N. Huan, W. J. Zheng, Y. J. Wang and H. T. Yuan, *J. Mater. Chem.*, 2012, **22**, 3699–3701.

46. M. M. Zhen, L. W. Su, Z. H. Yuan, L. Liu and Z. Zhou, *RSC Adv.*, 2013, **3**, 13696–13701.

47. S. M. Yuan, Z. Zhou and G. Li, *CrystEngComm.*, 2011, **13**, 4709–4713.

48. L. W. Su, Y. Jing and Z. Zhou, *Nanoscale*, 2011, **3**, 3967–3983.

49. C. T. Cherian, J. Sundaramurthy, M. Kalaivani, P. Ragupathy, P. S. Kumar, V. Thavasi, M. V. Reddy, C. H. Sow, S. G. Mhaisalkar, S. Ramakrishna and B. V. R. Chowdari, *J. Mater. Chem.*, 2012, **22**, 12198–12204.

50. M. J. Aragon, B. Leon, C. Perez Vicente and J. L. Tirado, *Inorg. Chem.*, 2008, **47**, 10366–10371.

51. M. M. Rahman, R. A. Rani, A. Sadek, A. S. Zoolfakar, M. Field, T. Ramireddy, K Kalantar-zadeh and Y. Chen, *J. Mater. Chem. A*, 2013, **1**, 11019–11025.

52. O. Delmer, P. Balaya, L. Kienle and J. Maier, *Adv. Mater.*, 2008, **20**, 501–505.

53. P. Balaya, H. Li, L. Kienle and J. Maier, *Adv. Funct. Mater.*, 2003, **13**, 621–625.

54. G. Li, X. L. Wang, Z. Chen, X. M. Ma and Y. F. Lu, *Electrochim. Acta,* 2013, **102**, 351–357.

55. S. Shi, P. Lu, Z. Liu, Y. Qi, L. G. Hector, H. Li and S. J. Harris, *J. Am. Chem. Soc.* 2012, **134**, 15476–15487.

56. C. Barchasz, J. C Lepretre, F. Alloin and S. Patoux, *J. Power Sources*, 2012, **199**, 322–330.

57. W. Y. Li, Q. F. Zhang, G. Y. Zheng, Z. W. Seh, H. B. Yao and Y. Cui, *Nano Letters*, 2013, **13**, 5534–5540.

58. J. Y. Choi, D. J. Lee, Y. M. Lee, Y. G. Lee, K. M. Kim, J. K. Park and K. Y. Cho, *Adv. Funct. Mater.*, 2013, **23**, 2108–2114.

59. L. W. Su, Z. Zhou and M. M. Ren, *Chem. Commun.*, 2010, **46**, 2590–2592.

60. M. M. Ren, Z. Zhen, X. P. Gao, W. X. Peng and J. P. Wei, *J. Phys. Chem. C.*, 2008, **112**, 5689–5693.

61. M. Takahashi, S. Tobishima, K. Takei and Y. Sakurai, *Solid State Ionics*, 2002, **148**, 283–289.

Figure Captions

Figure 1. XRD pattern (green: PDF 20-804) and crystal structure of Nb_2O_5 hierarchical structure.

Figure 2. XPS spectra of the Nb3d peaks (a), O1s peak (b) and Nb_2O_5 microsphere (c).

Figure 3. Typical SEM (a and b) and TEM (c and d) images of flower-like Nb_2O_5 nanostructures.

Figure 4. N_2 adsorption/desorption isotherm and Barrett-Joyner-Halenda (BJH) pore size distribution plot (inset) of Nb_2O_5.

Figure 5. Schematic formation process (a) and SEM images of the samples synthesized at 180°C for (b) 2 h, (c)8 h, (d) 16 h, and (e) XRD patterns of the as-prepared Nb_2O_5 products.

Figure 6. (a) Ultraviolet-visible diffusive absorption spectrum and insert is the plot of transformed Kubelka-Munk function versus the energy of the light absorbed. (b) Absorption spectra of a solution of RhB in the presence of Nb_2O_5 and under exposure to UV light, (c) time course of the decrease in the dye concentration using different catalysts, (d) Photodegradation of RhB by Nb_2O_5 catalyst under different solutions.

Figure 7. The typical charge/discharge curves (a) and CV curves (b) of Nb_2O_5, cycling performance for the Nb_2O_5 samples tested at a current density of 50 mAg^{-1} in the potential range of 0.01–3.0 V (c), and the rate capability of Nb_2O_5 electrode (d).

Figure 8. (a) Typical electrochemical impedance spectra, presented as Nyquist plots for the Nb_2O_5 electrodes and the equivalent circuit used to fit the EIS, (b) Nyquist plots of the Nb_2O_5 electrodes at different stages.

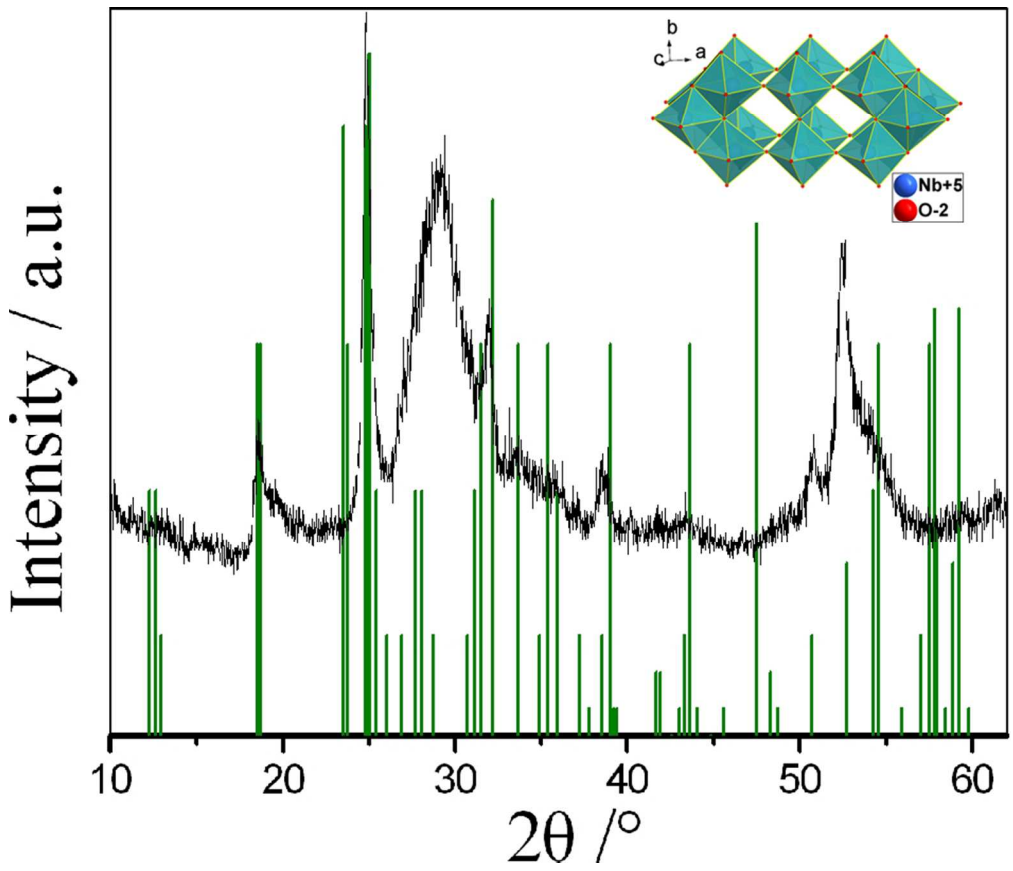

XRD pattern (green: PDF 20-804) and crystal structure of Nb2O5 hierarchical structure.
80x68mm (300 x 300 DPI)

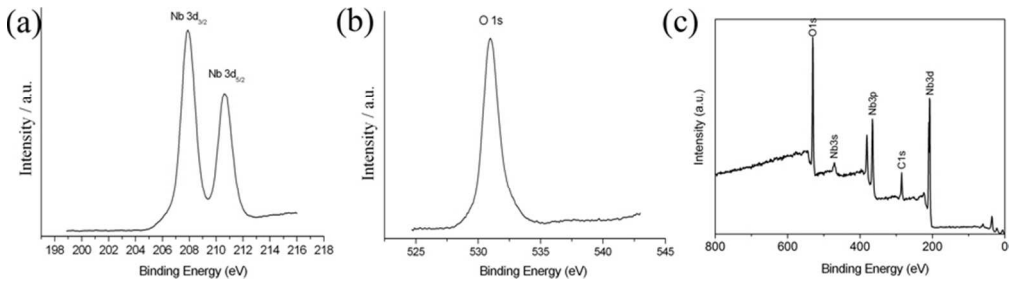

XPS spectra of the Nb3d peaks (a), O1s peak (b) and Nb2O5 microsphere (c).
80x21mm (300 x 300 DPI)

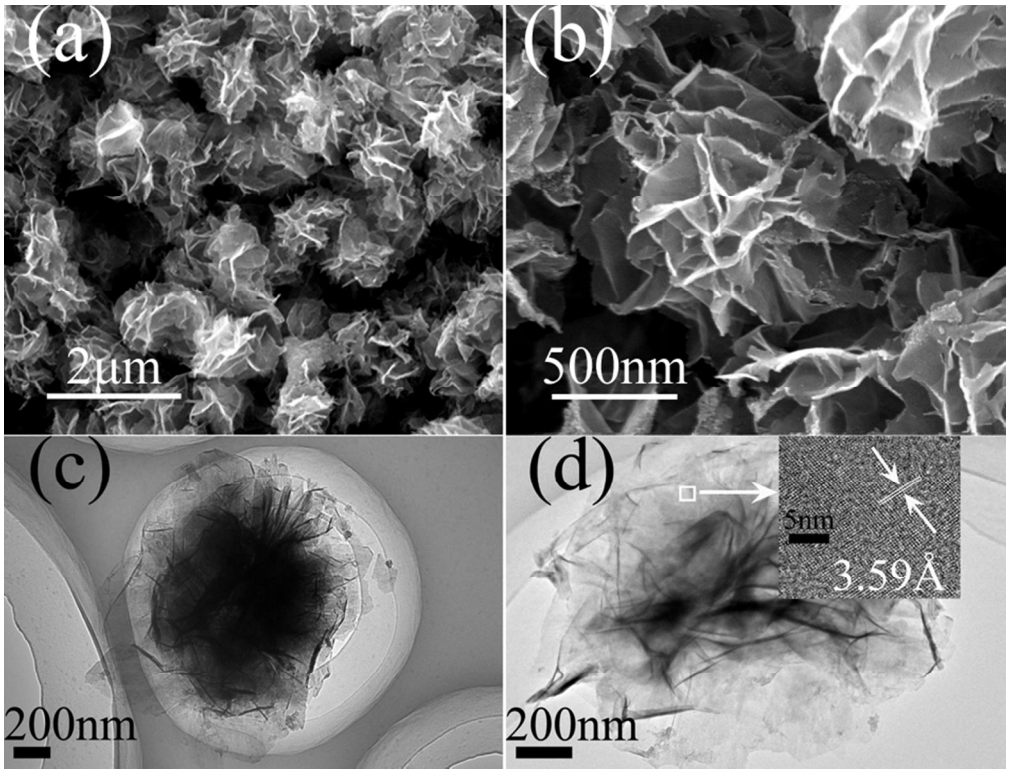

Typical SEM (a and b) and TEM (c and d) images of flower-like Nb2O5 nanostructures.
80x61mm (300 x 300 DPI)

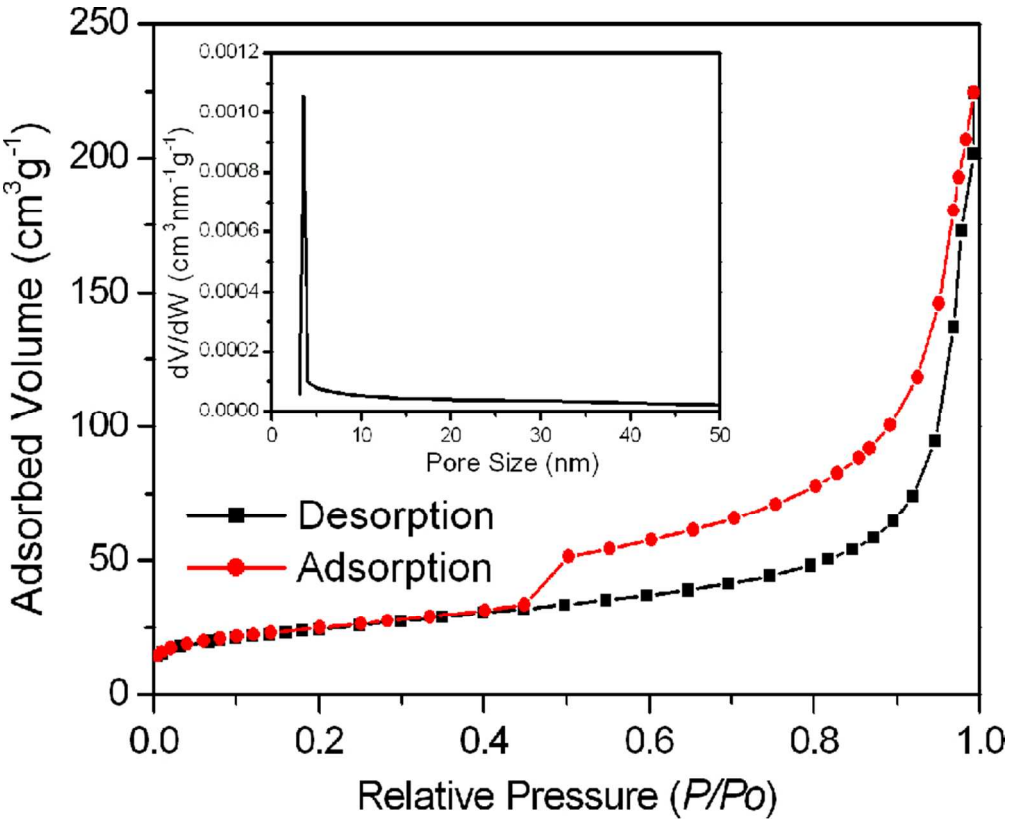

N2 adsorption/desorption isotherm and Barrett-Joyner-Halenda (BJH) pore size distribution plot (inset) of Nb2O5.
80x64mm (300 x 300 DPI)

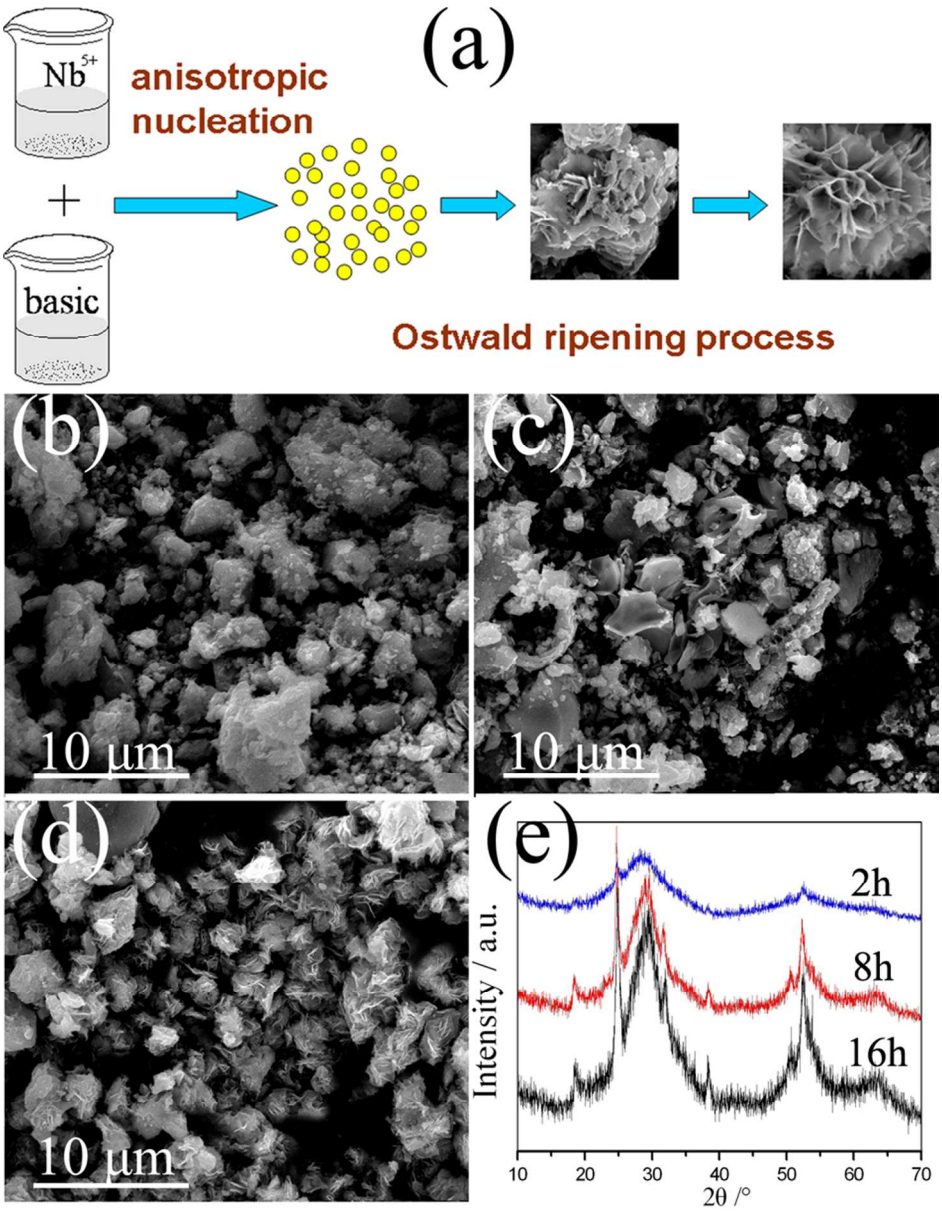

Schematic formation process (a) and SEM images of the samples synthesized at 180°C for (b) 2 h, (c)8 h, (d) 16 h, and (e) XRD patterns of the as-prepared Nb2O5 products.
80x102mm (300 x 300 DPI)

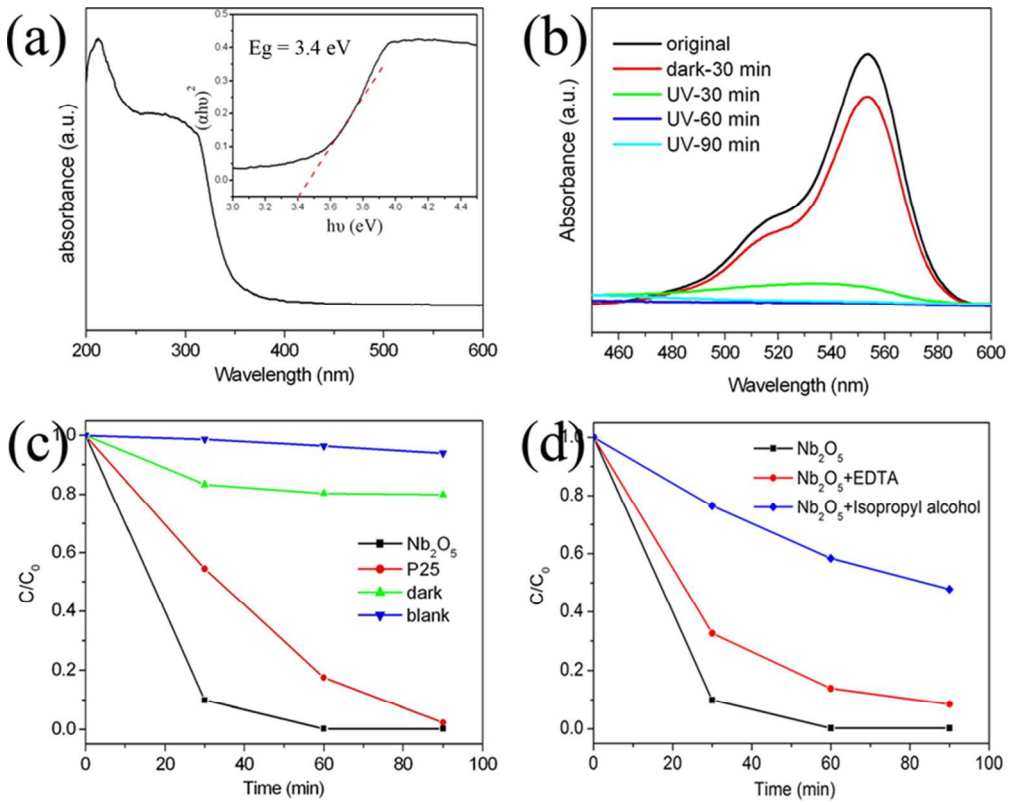

(a) Ultraviolet-visible diffusive absorption spectrum and insert is the plot of transformed Kubelka-Munk function versus the energy of the light absorbed. (b) Absorption spectra of a solution of RhB in the presence of Nb2O5 and under exposure to UV light, (c) time course of the decrease in the dye concentration using different catalysts, (d) Photodegradation of RhB by Nb2O5 catalyst under different solutions.
80x63mm (300 x 300 DPI)

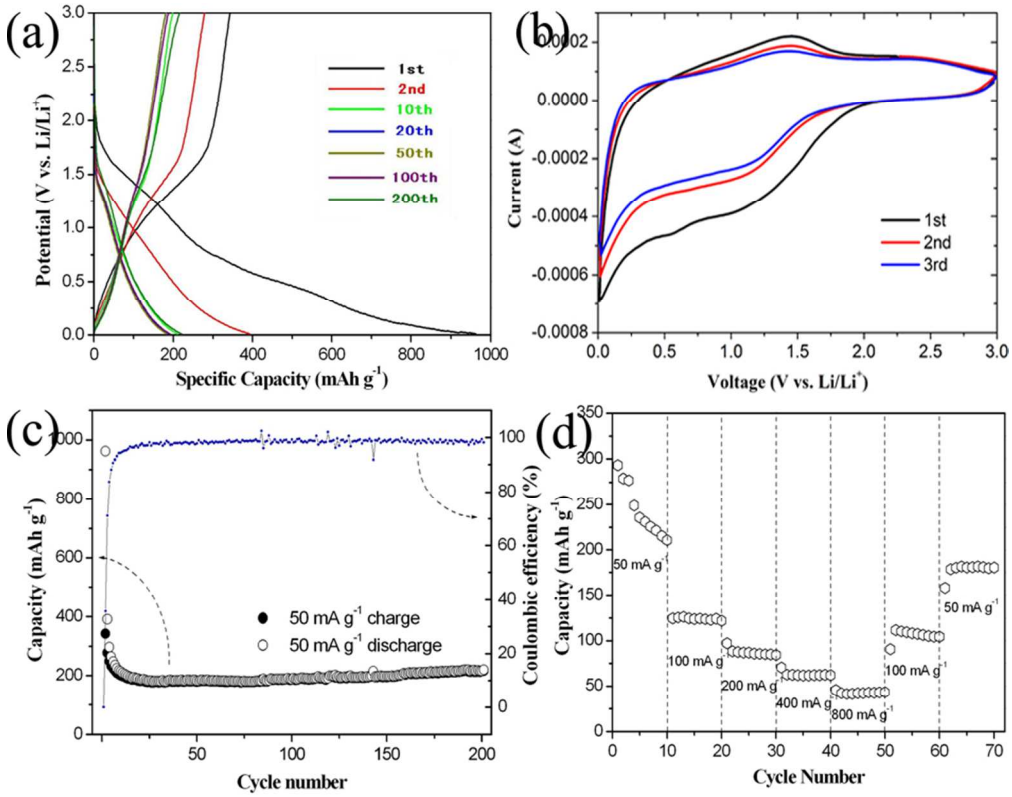

The typical charge/discharge curves (a) and CV curves (b) of Nb2O5, cycling performance for the Nb2O5 samples tested at a current density of 50 mAg-1 in the potential range of 0.01–3.0 V (c), and the rate capability of Nb2O5 electrode (d).
80x63mm (300 x 300 DPI)

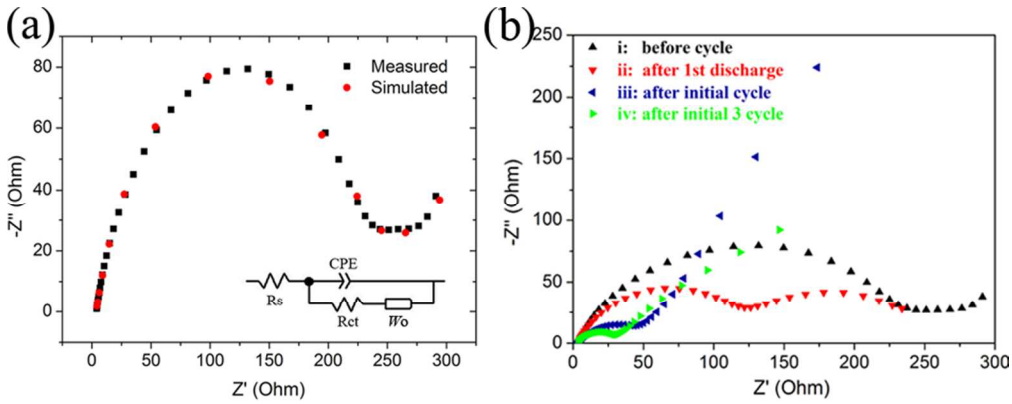

(a) Typical electrochemical impedance spectra, presented as Nyquist plots for the Nb2O5 electrodes and the equivalent circuit used to fit the EIS, (b) Nyquist plots of the Nb2O5 electrodes at different stages.
80x31mm (300 x 300 DPI)

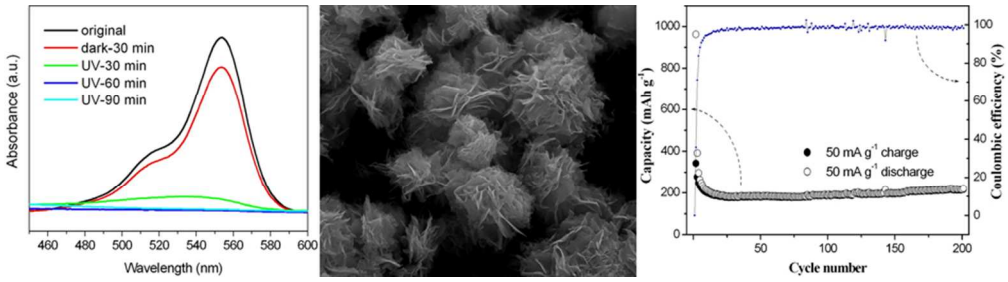

Graphical Abstract

80x21mm (300 x 300 DPI)